Water Research 122 (2017) 431–439

Contents lists available at ScienceDirect

Water Research

journal homepage: www.elsevier.com/locate/watres

# Holographic characterization of contaminants in water: Differentiation of suspended particles in heterogeneous dispersions

Laura A. Philips [a, *], David B. Ruffner [a], Fook Chiong Cheong [a], Jaroslaw M. Blusewicz [a], Priya Kasimbeg [a], Basma Waisi [b], Jeffrey R. McCutcheon [c], David G. Grier [d]

[a] Spheryx, Inc., 330 E. 38th St. #48J, New York, NY 10016, USA
[b] Inorganic Membrane, Department of Science and Technology, MESA+ Institute for Nanotechnology, University of Twente, Enschede, The Netherlands
[c] Department of Chemical & Biomolecular Engineering, Center for Environmental Sciences and Engineering, University of Connecticut, Storrs, CT 06269 USA
[d] Department of Physics and Center for Soft Matter Research, New York University, New York, NY 10003, USA

ARTICLE INFO

*Article history:*
Received 7 February 2017
Received in revised form
5 May 2017
Accepted 3 June 2017
Available online 7 June 2017

*Keywords:*
Holographic microscopy
Particle characterization
Concentration measurement
Colloid
Emulsion
Bacteria

ABSTRACT

Determining the size distribution and composition of particles suspended in water can be challenging in heterogeneous multicomponent samples. Light scattering techniques can measure the distribution of particle sizes, but provide no basis for distinguishing different types of particles. Direct imaging techniques can categorize particles by shape, but offer few insights into their composition. Holographic characterization meets this need by directly measuring the size, refractive index, and three-dimensional position of individual particles in a suspension. The ability to measure an individual colloidal particle's refractive index is a unique capability of holographic characterization. Holographic characterization is fast enough, moreover, to build up population distribution data in real time, and to track time variations in the concentrations of different dispersed populations of particles. We demonstrate these capabilities using a model system consisting of polystyrene microbeads co-dispersed with bacteria in an oil-in-water emulsion. We also demonstrate how the holographic fingerprint of different contaminants can contribute to identifying their source.



## 1. Introduction

Oil extraction and petroleum refining inevitably generate oily wastewater. With a production in excess of 200 million barrels per day, oily wastewater is the largest waste stream in the global oil and gas industry (Dal Ferro and Smith, 2007). Efforts to monitor and mitigate this source of environmental contamination are hindered by the tendency to form long-lived oil-in-water emulsions (Kokal et al., 2002; Khelifa et al., 2004; Yu et al., 2013). Increasingly strict regulation of oil concentration in effluent water (Yu et al., 2013) creates a need for methods to measure the size distribution and concentration of oil emulsion droplets. In-line and on-line monitoring have a particular need for measurement techniques that do not require post-installation calibration.

Mitigating oil-emulsion pollution by coagulation with microplastic beads creates an alternative risk of environmental contamination by the beads themselves. This compounds the challenge faced by wastewater treatment works of environmental microbeads arising from personal care products (Murphy et al., 2016).

Effectively monitoring the quality of effluent wastewater from oil refining and related industrial activities increasingly requires characterization methods that can differentiate dispersed colloidal particles on the basis of composition and then monitor the concentrations and size distributions of each component (Adin, 1999; Bramucci and Nagarajan, 2006; Levine et al., 1991; Muttamara, 1996). Complex heterogeneous mixtures from industrial and municipal effluents require multiple analytical techniques to identify the presence of different species (Levine et al., 1985). For suspended materials in particular, conventional particle-sizing techniques such as dynamic light scattering (DLS) (Goldburg, 1999; Xu, 2015), light obscuration (LO) (Hawe et al., 2013; Weinbuch et al., 2014), and the Coulter principle (Rhyner, 2011) offer insights into the distribution of particle diameters in aqueous solutions but are unable to distinguish particles made of different materials. Particle-shape analysis by micro-flow imaging (MFI) (Sharma et al., 2010) similarly cannot differentiate different types of

* Corresponding author.
*E-mail address:* lphilips@spheryx.solutions (L.A. Philips).

http://dx.doi.org/10.1016/j.watres.2017.06.006

emulsion droplets. Here, we demonstrate that images acquired through in-line holographic video microscopy (Sheng et al., 2006; Lee et al., 2007) can be interpreted with the Lorenz-Mie theory of light scattering (Bohren and Huffman, 1983; Mishchenko et al., 2001) to measure the sizes and refractive indexes of individual colloidal particles as they flow down a microfluidic channel (Lee and Grier, 2007; Cheong et al., 2009).

The ability to measure the refractive index of individual colloidal particles is a unique benefit of holographic characterization relative to other particle-characterization techniques (Xu, 2001; Lee et al., 2007). Because the refractive index can serve as a proxy for a particle's composition, this information is useful for differentiating co-dispersed populations of colloidal particles (Yevick et al., 2014). Simultaneous measurements of size and refractive index enable us to monitor the characteristics of different types of particles independently, and to monitor their concentrations over time.

## 2. Methods and materials

### 2.1. Methods

#### 2.1.1. Holographic characterization

Fig. 1 depicts the principle and workflow of a holographic characterization measurement. The custom-built instrument, shown schematically in Fig. 1 (a), illuminates its sample with the collimated beam from a solid-state laser (ThorLabs CPS532, 4.5 mW) operating at a vacuum wavelength of $\lambda = 532$ nm. Light scattered by a particle in the sample interferes with the unscattered portion of the laser beam in the focal plane of a telecentric microscope created with a standard microscope objective lens (Nikon Plan Fluor, 40×, numerical aperture 0.75) and a 200 mm focal length tube lens. The magnified interference pattern is relayed to a video camera (Allied Vision Mako U-130B) that records its intensity, $I(\mathbf{r})$, with an effective magnification of 120 nm/pixel on a 1280 pixel × 1024 pixel array.

Each video frame constitutes a hologram of the particles in the observation volume at the instant that the image was recorded. The example in Fig. 1(b) is a 200 pixel-wide region of interest cropped from the full field of view showing the experimentally recorded hologram of a polystyrene microbead dispersed in water. Each hologram is fit pixel-by-pixel to predictions of the Lorenz-Mie theory of light scattering to obtain the particle's instantaneous three-dimensional location, $\mathbf{r}_p$, its diameter, $d_p$, and its refractive index, $n_p$, at the imaging wavelength. Fig. 1(c) shows such a fit.

The quality of this typical fit can be appreciated by averaging the hologram over angles to obtain its radial profile, which is plotted as a black curve in Fig. 1(d). The corresponding radial profile of the fit is superimposed as an orange curve. The experimental and

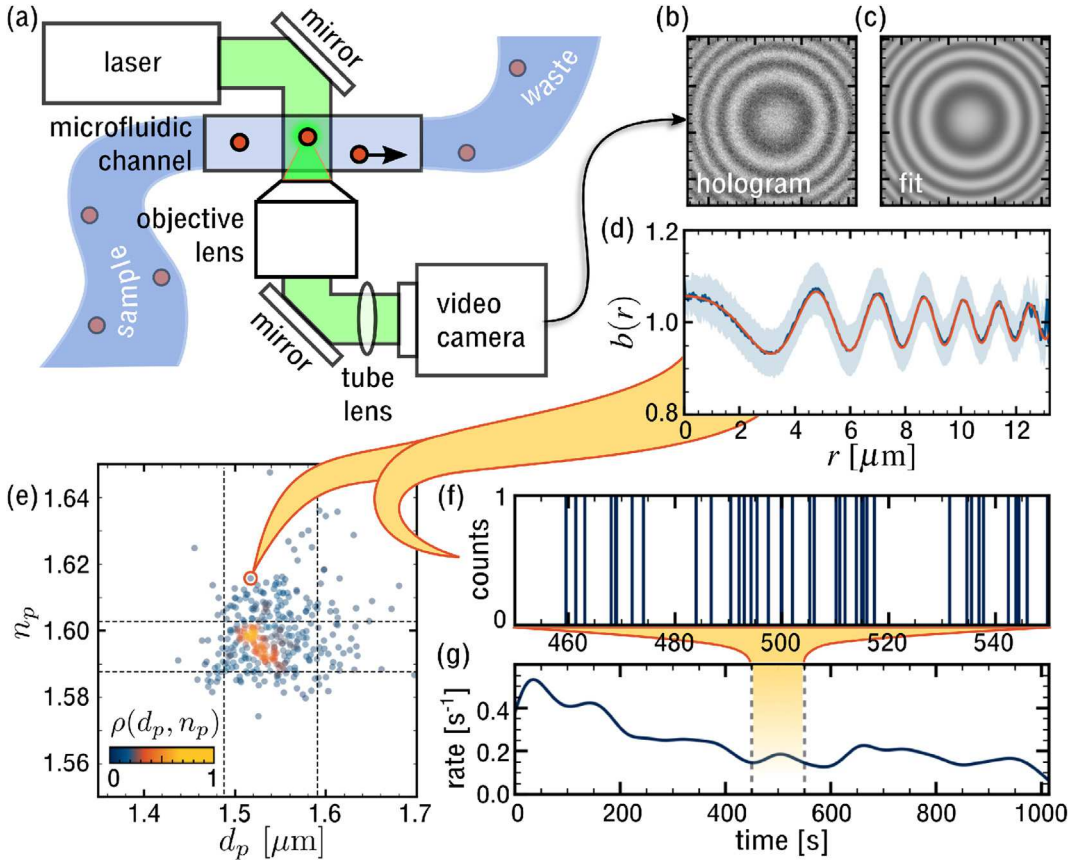


**Fig. 1.** Principle of holographic characterization. (a) Instrumentation. The sample containing suspended particles flows down a microfluidic channel, where it is illuminated by a collimated laser beam. Light scattered by a particle interferes with the rest of the beam in the focal plane of a microscope. The intensity of the magnified interference pattern is recorded by a video camera. (b) Detail from the normalized hologram, $b(\mathbf{r})$, of a polystyrene microbead in water. (c) Corresponding fit of the experimental hologram to predictions of the Lorenz-Mie theory of light scattering. (d) Radial profile, $b(r)$, of the experimental hologram (black) overlaid with the fit profile (orange) showing excellent agreement. The blue shaded region indicates instrumental uncertainty in $b(r)$. (e) Distribution of fit values of the diameter, $d_p$, and refractive index, $n_p$, of a sample of 361 NIST-traceable polystyrene spheres. Each plot symbol represents the properties of a single colloidal sphere, and has a size comparable to the uncertainty in the sphere's properties. Colors represent the local density of observations. Dashed lines represent the one-sigma confidence interval in the NIST-certified properties. (f) The arrival time of observations creates a time series of particle counts that can be converted into a time-resolved measurement of the concentration of particles dispersed in the known volume of flowing suspension. (For interpretation of the references to colour in this figure legend, the reader is referred to the web version of this article.)

theoretical curves agree to well within the instrumental uncertainty, which is indicated by the shaded blue region in Fig. 1(d). Each such fit provides characterization data for a single particle with instrumental uncertainties of $\Delta d_p = 6$ nm in the single-particle diameter and $\Delta n_p = 2 \times 10^{-3}$ in the refractive index.

Population averages for a sample, such as the example in Fig. 1(e), can be obtained by repeating this process as particles flow through the observation volume. The instrument in Fig. 1(a) is outfitted for this purpose with a microfluidic flow channel (ibidi, μ-Slide VI Luer Uncoated Microscopy Chamber). This 2 cm-long channel has an optical path length of 100 μm. Pressure-driven flows of up to 1 mm $s^{-1}$ are driven with a syringe pump (New Era Systems, NE-1000) These flows are fast enough to analyze 10 μL of sample in under 10 min, yet slow enough to avoid artifacts due to motion blurring (Cheong et al., 2009; Dixon et al., 2011b) given the camera's 50 μs exposure time.

The camera is set to record 50 frames per second, which means that each particle is recorded at least 5 times as it transits the observation volume. The resulting sequence of location measurements is linked into a trajectory for each particle using a maximum likelihood algorithm (Crocker and Grier, 1996; Cheong et al., 2009). Trajectories are used to monitor the flow profile within the channel (Cheong et al., 2009) so that the total volume of analyzed sample is known precisely. The characterization data associated with each trajectory are combined to improve the instrumental precision and accuracy of the single-particle characterization data. Data points in Fig. 1(e) were obtained in this way.

The density of points, $\rho(d_p, n_p)$, in a scatter plot such as Fig. 1(e) provide insight into the distribution of sizes and particle properties within the sample. The individual data points in Fig. 1(e) are colored according to $\rho(d_p, n_p)$ to avoid ambiguity due to points overlapping and obscuring each other. The data in this plot suggest that this sample has a mean particle diameter of $\overline{d}_p = 1.53 \pm 0.02$ μm and a mean refractive index of $\overline{n}_p = 1.595 \pm 0.002$. The former is consistent with the size range certified by the National Institutes of Science and Technology (NIST), as quoted by the manufacturer. The latter is consistent with the range expected for polystyrene spheres (Kasarova et al., 2007) at the imaging wavelength, which is plotted as horizontal dashed lines in Fig. 1(e).

The number of individual single-particle characterization results that fall outside the manufacturer's specification is smaller than would be expected on the basis of simple counting statistics. Our results therefore suggest that the quality of the sample actually surpasses the manufacturer's specification. Similarly good results are obtained with validation measurements on standard samples with diameters ranging from 400 nm to 20 μm and with refractive indexes ranging from 1.35 to 2.1.

Both the number of particles and the volume of sample analyzed are known precisely in a holographic characterization measurement. These data therefore can be used to measure the concentration of particles in suspension. This can be reported as an overall value for the entire sample using the aggregated data in Fig. 1(e). Alternatively, the time sequence of particle detections can be used to monitor fluctuations in particle concentration. Fig. 1(f) shows a 1.7 min series of detections from a 17 min measurement. Smoothing these data, as in Fig. 1(g), shows an overall rate of 1 particle detection every 5 s in this sample.

### 2.1.2. Holographic characterization: Lorenz-Mie analysis

The hologram of a colloidal particle recorded by the camera may be modeled as the superposition of the incident illumination, $\mathbf{E}_0(\mathbf{r})$, and the wave scattered by the particle, $\mathbf{E}_s(\mathbf{r})$:

$$I(\mathbf{r}) = \left|\mathbf{E}_0(\mathbf{r}) + \mathbf{E}_s(\mathbf{r})\right|^2. \tag{1}$$

We model the illumination's electric field as a plane wave propagating along $\hat{z}$ and linearly polarized along $\hat{x}$,

$$\mathbf{E}_0(\mathbf{r}) = E_0 e^{ikz}\hat{x}, \tag{2}$$

where $k = 2\pi n_m/\lambda$ is the wavenumber of light in a medium of refractive index $n_m$. The field scattered by a sphere at position $\mathbf{r}_p$ then has the form

$$\mathbf{E}_s(\mathbf{r}) = E_0(\mathbf{r}_p)\, \mathbf{f}_s\big(k(\mathbf{r}-\mathbf{r}_p)\big|d_p, n_p\big), \tag{3}$$

where $\mathbf{f}_s(k\mathbf{r}|d_p, n_p)$ is the Lorenz-Mie scattering function for a sphere of diameter $d_p$ and refractive index $n_p$ illuminated by an $\hat{x}$-polarized plane wave. This function is a standard result in the theory of light scattering (Bohren and Huffman, 1983; Mishchenko et al., 2001), and can be computed efficiently (Wiscombe, 1980; Yang, 2003; Pena and Pal, 2009; Neves and Pisignano, 2012). Treating the microscope's focal plane as $z = 0$ and normalizing a measured hologram by the illumination's intensity, $I_0 = \left|E_0\right|^2$, yields

$$b(\mathbf{r}) \equiv \frac{I(\mathbf{r})}{I_0} = \left|\hat{x} + e^{-ikz_p}\, \mathbf{f}_s\big(k(\mathbf{r}-\mathbf{r}_p)\big|d_p, n_p\big)\right|^2. \tag{4}$$

We use the Levenberg-Marquardt algorithm (Markwardt, 2009) to fit this model pixel-by-pixel to the measured hologram by optimizing $\mathbf{r}_p$, $d_p$ and $n_p$. In practice, we also subtract the camera's dark count, $I_d$, from $I(\mathbf{r})$ and $I_0$ before computing the normalized hologram. The holograms in Fig. 1(b) and (c) were treated in this way.

### 2.1.3. Holographic characterization: calibration

Holographic characterization relies on three calibration constants: the vacuum wavelength of the illumination, the magnification of the optical train, and the refractive index of the fluid medium at the imaging wavelength. The laser wavelength is specified by the manufacturer with part-per-thousand precision, which is sufficient for holographic characterization measurements. The microscope's magnification of 120 nm/pixel is computed from the magnification of the objective lens, the focal length of the tube lens, and the manufacturer's specification for the camera's pixel dimensions. The resulting value is confirmed with a magnification calibration scale (Ted Pella, catalog number 2285-16) These two instrumental parameters can be assessed once and do not require subsequent calibration.

The third sample-dependent parameter can be measured separately, for instance with an Abbe refractometer. No other calibration constants or procedures are required.

### 2.1.4. Holographic characterization: operating range, precision and accuracy

Our implementation of holographic characterization works for particles ranging in diameter from 400 nm to 20 μm. The lower limit is set by the low signal-to-noise ratio of scattering patterns created by smaller particles. The upper limit is set by the appearance of strong local minima in the five-dimensional error surface for the nonlinear fit. Optimization algorithms based on gradient descent, such as Levenberg-Marquardt, can become trapped in these local minima, and thus yield incorrect results. This limitation may be lifted in future implementations by adopting alternative optimization strategies.

Estimates for $\mathbf{r}_p$, $d_p$ and $n_p$ obtained by fitting measured

holograms to Eq. (4) include computed uncertainties in these adjustable parameters. If the reduced $\chi^2$ statistic for the fit is close to unity, these uncertainties should serve as estimates for the precision in each parameter. Previous studies (Lee et al., 2007; Cheong et al., 2009; Krishnatreya et al., 2014) have confirmed this assessment by measuring the trajectories of freely diffusing colloidal spheres. Random measurement errors contribute a constant additive offset to a trajectory's mean-squared displacement that can be extracted from the computed results. Such measurements confirm that the precision for measuring a micrometer-scale sphere's location is ±1 nm in plane and ±3 nm along the optical axis. Agreement between results obtained in each of the three Cartesian coordinates suggests that the measurement's accuracy is comparable to its precision (Krishnatreya et al., 2014). Measurements of single-particle sedimentation yield estimates for particles' hydrodynamic radii that are consistent with holographic estimates, and support an overall precision of ±5 nm in particle diameter (Krishnatreya et al., 2014). Measurements performed with colloidal spheres dispersed in precision index-matching fluids (Shpaisman et al., 2012) suggest that the uncertainty in holographic estimates for the refractive index is ±0.002 refractive index units.

Although these error estimates were performed for homogeneous colloidal spheres, comparably good results have been obtained for porous spheres (Cheong et al., 2011), dimpled spheres (Hannel et al., 2015), and randomly branched fractal aggregates (Wang et al., 2016b, a). We anticipate, therefore, that holographic characterization will perform comparably well for assessing particle composition characteristics in wastewater analysis and environmental monitoring.

#### 2.1.5. Holographic characterization: concentration range

The upper range of particle concentrations amenable to holographic characterization is set by the need to avoid excessive overlap between neighboring particles' holograms. As a rule of thumb, this limit is reached when more than ten particles are in the observation volume at once, and corresponds to a concentration of $10^7$ particles/mL for our instrument. The lower limit is set by the need for particles to pass through the observation volume during a reasonable measurement period. Requiring 100 particles to pass through during a 10 min measurement sets the lower limit of the concentration range to $10^3$ particles/mL.

For crude-oil emulsions, the upper accessible concentration range corresponds to 20 mg $L^{-1}$ of 1 μm diameter droplets and $2 \times 10^4$ mg $L^{-1}$ of 10 μm diameter droplets. This is suitable for verifying compliance with current regulatory limits for effluent wastewater of 10 mg $L^{-1}$ in China (Yu et al., 2013) and 5 mg $L^{-1}$ in the United States (Office of Water (4303T), 2004).

#### 2.1.6. Holographic characterization: aspherical particles

The Lorenz-Mie analysis used for holographic particle characterization presupposes that each particle is a homogeneous, isotropic and smooth sphere. Applying the same analysis to holograms of aspherical and inhomogeneous particles yields results for the diameter and refractive index that can be interpreted with effective medium theory (Aspnes, 1982). Specifically, recent studies have demonstrated (Wang et al., 2016a) that holographic characterization of non-ideal particles yields the size of an effective sphere that bounds the particle. The estimated refractive index is the volume-weighted average of the material from which the particle is composed and the medium that fills its pores. This analysis has been shown to yield useful results for dimpled spheres (Hannel et al., 2015), rough spheres (Hannel et al., 2015), porous spheres (Cheong et al., 2011), and aspherical fractal clusters (Wang et al., 2016a, b).

#### 2.1.7. Dynamic light scattering

Dynamic light scattering measurements are performed with a Malvern Zetasizer Nano ZS. Samples are mixed by manual agitation before being transferred to a 12 mm square polystyrene cuvette (Malvern DTS0012) for measurement. Intensity-averaged particle diameters were calculated from the instrument's standard cumulant analysis, as defined in ISO13321.

### 2.2. Materials

#### 2.2.1. Monodisperse colloidal spheres

All of the monodisperse colloidal spheres used for this study were purchased as aqueous dispersions from Bangs Laboratories.

Polystyrene size standards (Catalog Number NT16N) have a NIST-certified diameter of $d_p = 1.54 \pm 0.01$ μm. They were delivered at a volume fraction of 1%. This sample was diluted with deionized (DI) water to a volume fraction of $10^{-6}$ before use.

Three populations of microspheres were combined to create the three-component mixture used for Fig. 2: silica microspheres (Catalog Number SS03N, $d_p = 0.69$ μm); polymethylmethacrylate (PMMA) microspheres (Catalog Number PP03N, $d_p = 0.71$ μm); and polystyrene microspheres (Catalog Number NT12N, $d_p = 0.70$ μm). Each of these samples were delivered at 10 % wt/v and were individually diluted with DI water to a concentration of $10^7$ particles/mL. Equal volumes of the three diluted samples then were mixed to create the three-component sample. The same mixture was used for DLS and holographic characterization measurements. The specified diameter of the PMMA particles was established with dynamic light scattering (DLS). The equivalent values for the silica and polystyrene particles were determined with a combination of

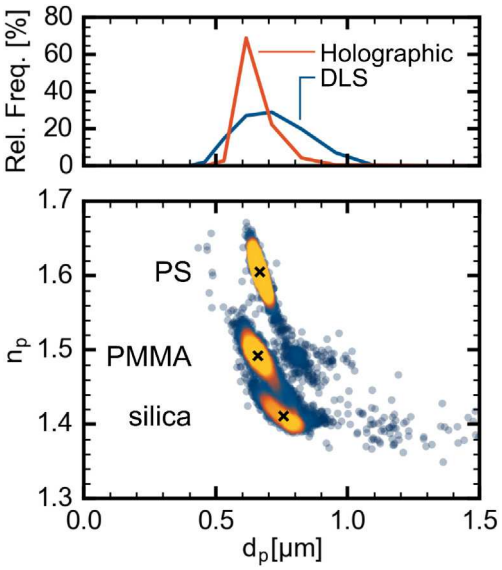


**Fig. 2.** Comparison of holographic characterization and DLS analysis of a heterogeneous colloidal dispersion created as a mixture of three distinct populations of colloidal spheres. (Upper panel) DLS and holographic characterization yield consistent results for the size distribution of particles in suspension. This one-dimensional view, however, does not identify the different components in the mixture. (Lower panel) Holographic characterization clearly resolves three peaks in the joint distribution of particle diameters and refractive indexes. Plot symbols are colored by the relative probability density, $\rho(d_p, n_p)$, of observing particles with diameter $d_p$ and refractive index $n_p$. Peaks appear as yellow clusters in this scatter plot. Superimposed symbols (x) indicate cluster-averaged properties of the three distinct populations. The holographic characterization data in the upper panel were obtained by averaging these discrete measurement over $n_p$, thereby eliminating information about particle composition. (For interpretation of the references to colour in this figure legend, the reader is referred to the web version of this article.)

photon correlation spectroscopy (PCS) and quasi-elastic light scattering (QELS).

#### 2.2.2. Silicone oil emulsion

Silicone oil was obtained from Dow Corning (SYLGARD 184 Silicone Elastomer, Lot #0008569647). Oil was dispersed in DI water at a concentration of 1 mg $mL^{-1}$ by vortexing for 5 min. These samples were then agitated by hand up to the point that the sample was introduced into the instrument for measurement.

#### 2.2.3. E. coli suspension

*Escherichia coli* is a rod-like bacterium with a cylindrical diameter of about 0.8 μm and a length that ranges from 1 μm to somewhat less than 4 μm depending on the time since the last cell division (Berg, 2004). Samples of *Escherichia coli* K-12 were obtained from Carolina Biological Supply Company and were cultured at 37 °C in LB Broth obtained from ThermoFisher Scientific. Cultured bacteria were dispersed for study in DI water at 24 °C at a concentration of $10^6$ bacteria/mL.

#### 2.2.4. Crude oil emulsions

Crude oil samples were obtained from ONTA, Inc. (Light Crude Oil Set). Emulsion of these samples were prepared and handled in the same manner as the silicone oil emulsions, at a concentration of 1 mg $mL^{-1}$.

## 3. Results and discussion

### 3.1. Validation with standard samples

The data in Fig. 1(e) were obtained with a dispersion of NIST-traceable colloidal size standards with a nominal diameter of $d_p = 1.54 \pm 0.05$ μm. This range is indicated by vertical dashed lines in Fig. 1(e). These particles are made of polystyrene, which has a refractive index of $n_p = 1.59 \pm 0.02$ at the imaging wavelength, as indicated by horizontal dashed lines. The specified standard deviations in size and refractive index establish a rectangular domain in the $(d_p, n_p)$ plane within which 68% of measured data points are expected to fall. In fact, 252 of the 361 measurements fall within this domain, or 70%. We conclude that the manufacturer's specification is consistent with the standard deviation of an assumed normal size distribution.

The data in Fig. 2 demonstrate that holographic characterization achieves comparably good results for heterogeneous samples that span a range of refractive indexes. In this case, the sample comprises three populations of monodisperse spheres, all of nearly the same size but composed of different materials. Three peaks are clearly resolved in the joint distribution, $\rho(d_p, n_p)$, of size and refractive index. The peak positions in this trimodal distribution are marked with plot symbols in Fig. 2 and agree with the manufacturer-specified properties of each of the component populations. Holographic characterization thus successfully differentiates the particles by composition, even when they cannot be differentiated by size.

Fig. 2 also compares results from holographic characterization with results obtained with dynamic light scattering for the same mixed sample. To make this comparison, the joint distribution of size and refractive index measured by holographic characterization is averaged over refractive indexes and distributed into the same diameter bins presented by the commercial DLS software. The trimodal data in the scatter plot therefore appears as a single peak in the relative frequency of particle diameters. This peak coincides well with the peak in the size distribution reported by DLS, thereby providing additional verification of the size data obtained holographically.

DLS offers no basis for differentiating particles by composition. The slight discrepancy in the widths of the peaks can be ascribed to the range in the particles' refractive indexes, which is not taken into account by DLS. The existence of the underlying trimodal composition could not have been inferred from DLS data, although it is obvious in the holographic characterization results. This, therefore, constitutes a distinctive benefit of holographic characterization for characterizing inhomogeneous samples.

### 3.2. Concentration measurements

By detecting and characterizing particles one at a time, holographic characterization also lends itself to measuring the concentration of particles and droplets in a suspension. This process could be subject to biases if the ability to detect and count particles somehow depended on the concentration. The data in Fig. 3(a) show the measured concentration of 1.5 μm-diameter polystyrene spheres in water over a range of $10^3$ particles/mL to $10^7$ particles/mL. Samples were prepared by repeated diluting an initial stock sample by ten-fold increments. Concentrations obtained by holographic characterization agree with the expected values over the entire range of concentrations.

Particle-resolved characterization also has the benefit that characterization results do not depend on particle concentration, even for heterogeneous samples. Fig. 3(b) compares results for 700 nm-diameter spheres obtained with holographic characterization and with DLS for the same colloidal mixture used for Fig. 2. The two measurement techniques agree well with the manufacturer's specification at $10^7$ particles/mL. Holographic characterization also reports consistent results down to concentrations as low as $10^3$ particles/mL. DLS, by contrast, deviates substantially from the correct value at lower concentrations. Similar concentration-dependent deviations in DLS results have been reported previously (Tomaszewska et al., 2013; Panchal et al., 2014).

### 3.3. Differentiating contaminants in a heterogeneous sample

The data in Fig. 4 illustrate how the size- and refractive-index data provided by particle-resolved holographic characterization can be used to differentiate different types of colloidal contaminants simultaneously dispersed in water. The model sample in this case contains a combination of polystyrene spheres, which resemble waterborne latex microbeads, as well as oil emulsion droplets and bacteria. Holographic characterization data for the three independent component samples are presented in Fig. 4(a) through Fig. 4(c).

The data for polystyrene microbeads in Fig. 4(a) show a small range of particle diameters and refractive indexes. The mean refractive index $n_p = 1.595 \pm 0.007$ is consistent with that of polystyrene (Kasarova et al., 2007). Silicone oil emulsion droplets are drawn from a much broader distribution of sizes, as can be seen in Fig. 4(b), but have a comparably narrow range of refractive indexes. This distribution, characteristic of emulsions, reflects the fact that each droplet has a homogeneous composition that is independent of size.

Bacteria, shown in Fig. 4(c), display substantially more variation in optical properties with size. The most probable refractive index, $n_p = 1.38 \pm 0.01$, at a diameter around $d_p = 1$ μm is consistent with results of previous studies (Liu et al., 2016). Smaller bacteria display higher effective refractive indexes because their light scattering properties are more strongly influenced by their high-index membranes (Liu et al., 2014). Larger, older bacteria have lower apparent refractive indexes because their rod-like morphology distorts their holograms, as can be seen in Fig. 4. Fitting such holograms to the Lorenz-Mie theory for spheres has been shown to

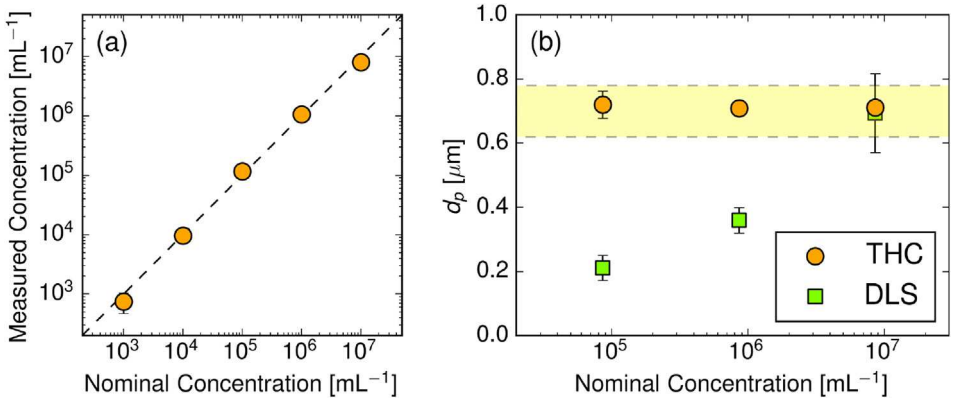


**Fig. 3.** Holographic measurements of particle concentration. (a) Measured concentrations of monodisperse silica spheres in water agrees with expected values for concentrations ranging from $10^3$ particles/mL to $10^7$ particles/mL. (b) Holographically-measured particle characteristics (circles) are independent of particle concentration and are consistent with the manufacturer's specification, indicated by the shaded region. Results obtained with dynamic light scattering (squares) deviate substantially at low particle concentration.

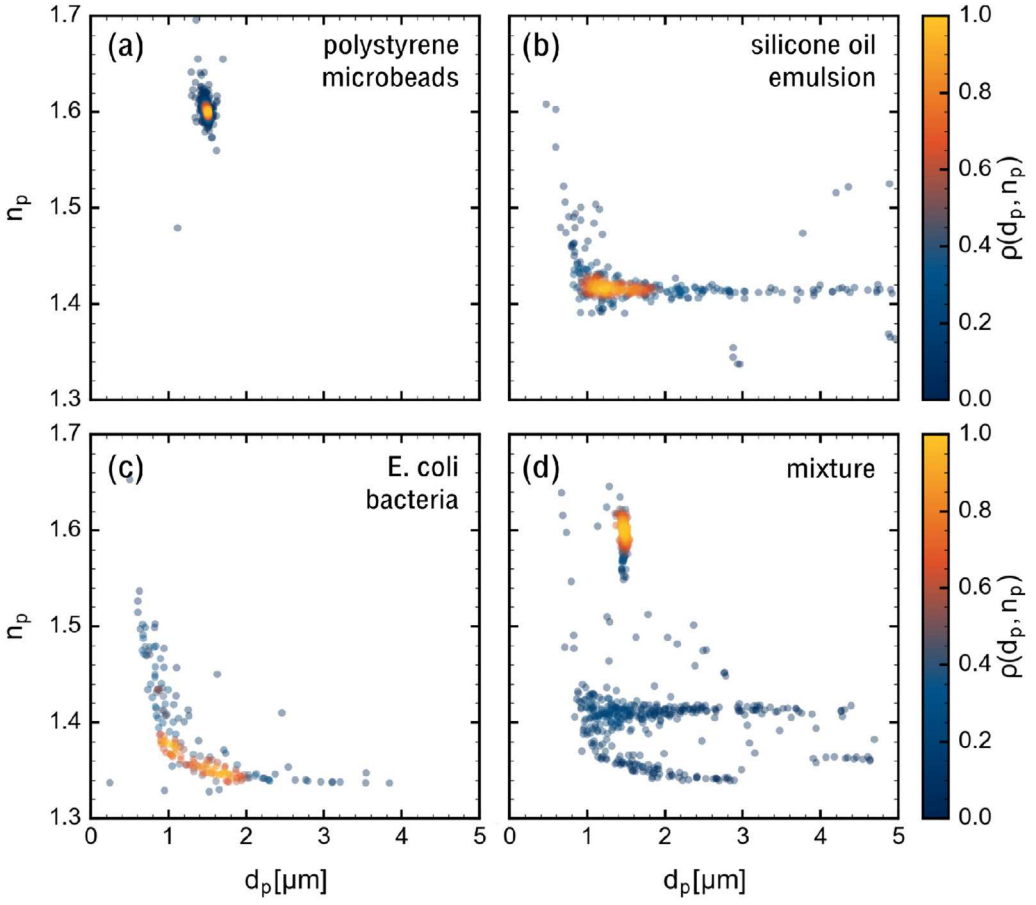


**Fig. 4.** Differentiating multiple contaminants in aqueous suspensions. (a) Polystyrene microbeads. (b) Silicone oil emulsion. (c) Bacteria. (d) Mixture of the samples from (a), (b) and (c) displaying signatures of all three populations of particles.

yield reliable values for the semi-major axis, but systematically lower values for the effective refractive index (Wang et al., 2016b). The observed distribution of properties, nevertheless, is characteristic of rod-like samples in suspension (Wang et al., 2016a).

The mixture of microbeads, oil emulsion and bacteria presented in Fig. 4(d) is intended to illustrate the utility of holographic characterization for assessing the nature and quantity of contaminants in wastewater. The three different populations' holographic signatures are clearly distinguishable in the joint distribution of particle size and refractive index. To the best of our knowledge, no other particle-characterization technique provides the information needed to simultaneously analyze multiple components that make up such a heterogenous system.

Holographic characterization cannot distinguish different types of particles that have the same size and the same refractive index. Such an overlap is apparent in Fig. 4(d) for 1 μm-diameter particles

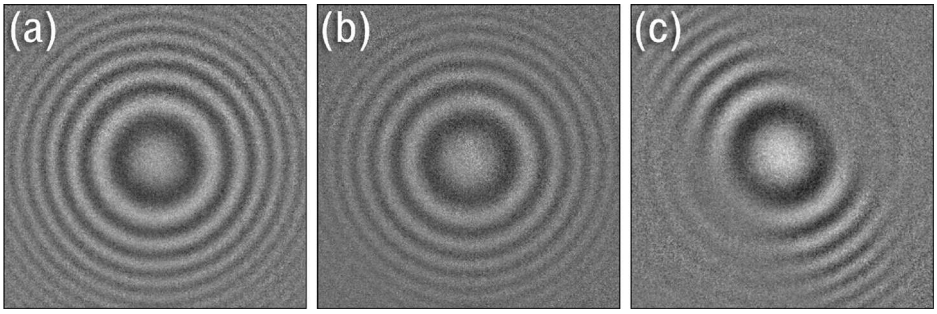


**Fig. 5.** Comparison of recorded holograms of (a) a polystyrene microbead, (b) an oil droplet and (c) a rod-like bacterium. The microbead in (a) can be distinguished form the oil droplet in (b) only through quantitative analysis. Anisotropy in the bacterium's hologram offers insights into its morphology.

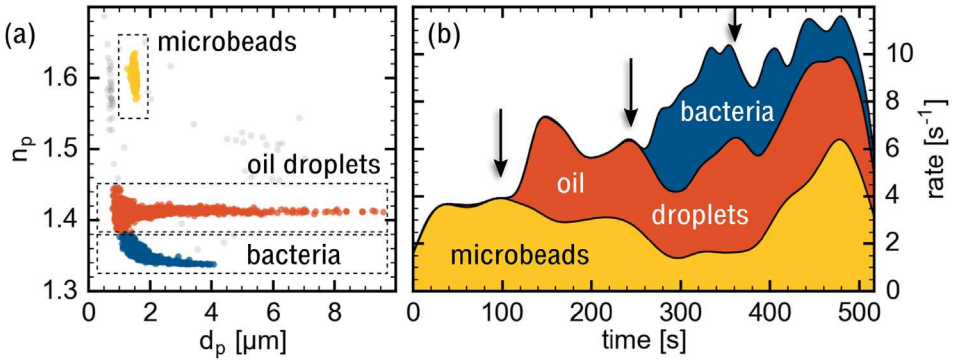


**Fig. 6.** Monitoring the concentration of microbeads, oil emulsion droplets and bacteria in a continuous stream. (a) Scatter plot of individual particles' diameters and refractive indexes, colored by category. Yellow: polystyrene microbeads; Red: silicone oil droplets; Blue: bacteria. The domain defined for each category is outlined with a dashed rectangle. (b) Rate of observations as a function of measurement time. Oil emulsion was added to the stream at 100 s, bacteria were added to the stream at 240 s, and more microbeads were added at 360 s. (For interpretation of the references to colour in this figure legend, the reader is referred to the web version of this article.)

with a refractive index around 1.4. In some cases, such degeneracies can be lifted by considering particle morphology (Wang et al., 2016b, a) as well as size and refractive index. This information also can be extracted from single-particle holograms, albeit at the cost of additional computational analysis (Cheong and Grier, 2010; Dixon et al., 2011a; Wang et al., 2016b, a). Fig. 5 illustrates this additional capability of holographic characterization through a comparison among typical holograms recorded for a polystyrene microbead (Fig. 4(a)), an oil droplet (Fig. 4(b)) and a bacterium (Fig. 4(c)). The rod-like morphology of the bacterium is evident in the uniaxial distortion of its hologram. Even without considering morphology, however, the presence of multiple overlapping populations in Fig. 4 can be inferred from trends in the distribution of properties in the $(d_p, n_p)$ plane.

### 3.4. Monitoring time-dependent concentrations

A typical distribution of particle properties, such as the example in Fig. 6(a) can be built up, particle-by-particle, over the course of 10 min. Any pattern of clustering in the distribution can serve as a

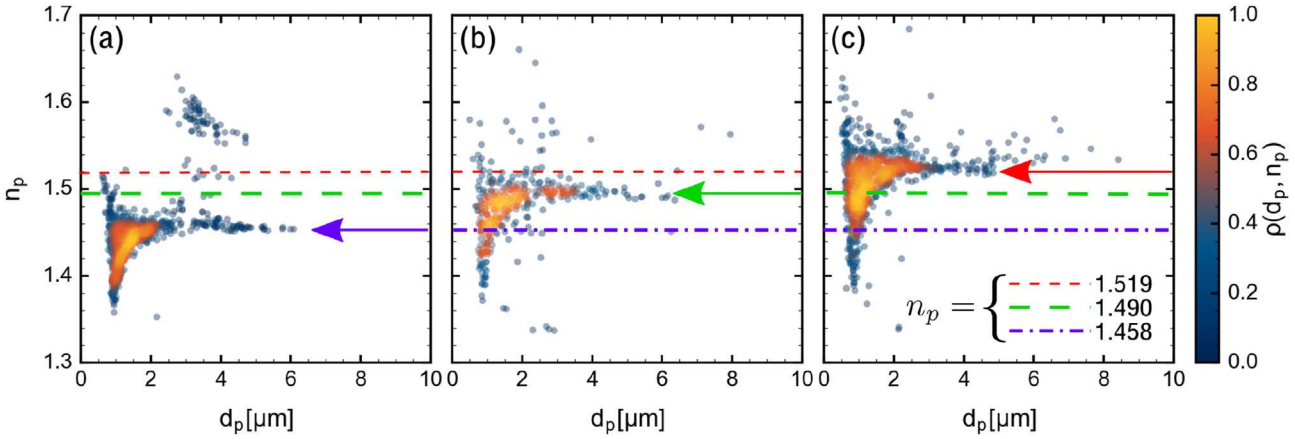


**Fig. 7.** Holographic characterization of crude oil emulsion droplets in water. (a) Pennsylvania light crude oil. (b) Bryan Mound sweet crude oil MLI001. (c) Basrah light crude oil OGJ 99. Horizontal dashed lines are guides to the eye to aid in comparing the characteristic refractive indexes for each sample.

template for differentiating the detected particles into different categories. The sample in Fig. 6(a), for example, displays the three clusters of points, distinguished by color, that are characteristic of monodisperse polystyrene microbeads, oil emulsion droplets and bacteria. Each data point, therefore, can be assigned a category as it arrives and used to compute the rate of arrival of that type of particle. This rate, in turn, yields an estimate for the instantaneous concentration for that category.

The traces in Fig. 6(b) chronicle the arrival rate of microbeads, oil droplets and bacteria in an sample stream that was deliberately modified in three stages to illustrate the monitoring capabilities of holographic characterization. Initially, the sample consisted only of a suspension of microbeads, with a mean arrival rate of 2 particles/s, which corresponds to a concentration of $2 \times 10^4$ particles/mL. After 100 s, silicone oil emulsion was injected into the flow. The observed concentration of oil droplets soon rises to $2 \times 10^4$ droplets/mL while the concentration of microbeads decreases slightly due to dilution. This process is repeated after 240 s with the addition of bacteria. The observed concentration of bacteria rises shortly thereafter, as the concentrations of oil droplets and microbeads both diminish. Finally, more microbeads are added to the stream at 360 s, increasing their total concentration to $3 \times 10^4$ particles/mL. Both bacteria and oil droplets are diluted by the added volume of solvent, and their concentrations decline.

This proof-of-principle measurement demonstrates that time-resolved holographic characterization can be used to track the concentrations of multiple components independently and simultaneously in heterogeneous sample streams. This unique capability of holographic characterization should be useful for monitoring wastewater quality and for identifying changes in solvent reclamation processes.

The quality of the differentiation depends on the sophistication of the classification scheme. As many as 5% of the bacteria may have been misclassified as oil droplets by the simple rectangular classification scheme used in Fig. 6. A smaller percentage of oil droplets might have been misclassified as bacteria. Additional data, such as morphological information, can be brought into consideration for cases where even more stringent differentiation is required.

### 3.5. Real-world samples: distinguishing crude oil emulsions

Holographic particle characterization offers insights into the nature of waterborne contaminants that can be useful for identifying the nature of the contamination. Fig. 7 shows holographic characterization results for aqueous emulsions of three different types of crude oil: Pennsylvania light (Fig. 7(a)), Bryan Mound sweet MLI001 (Fig. 7(b)) and Basrah light OGJ 99 (Fig. 7(c)). Crude oil being a complex material, the emulsion droplets display a complicated distribution of properties. In all three cases, the majority of droplets are drawn from a relatively narrow distribution of refractive indexes. This characteristic refractive index, moreover, is quite distinct for the three types of oil. Pennsylvania light crude has the lowest characteristic refractive index, $n_p = 1.46 \pm 0.01$. Droplets of Bryan Mound sweet scatter light more strongly, and have a significantly high characteristic refractive index, $n_p = 1.49 \pm 0.01$. Basrah light crude has the highest refractive index, $n_p = 1.52 \pm 0.01$. The horizontal dashed lines in Fig. 7 indicate these three values, and demonstrate that the three types of oil have easily distinguishable properties.

Light scattering by the smallest detectable particles is strongly influenced by their surface properties. Natural surfactants and surface-bound nanoparticles therefore contribute to the large spread in measured refractive indexes for the smallest particles, both above and below the characteristic value. Characteristic refractive indexes are most readily determined, therefore, by considering larger particles whose refractive indexes are dominated by their bulk properties.

The small proportion of high-index particles outside of the main distributions in Fig. 7 may reflect the influence of strongly absorbing soot-like components of the oil. A detailed analysis of these contaminants' influence on crude oil's holographic signature would be an interesting subject for future study.

## 4. Conclusions

We have demonstrated the use of holographic video microscopy for analyzing micrometer-scale colloidal particles dispersed in aqueous media. Fitting holograms of individual particles to predictions of the Lorenz-Mie theory of light scattering yields measurements of the size and refractive index of each particle passing through the sample volume. This information can be used to differentiate colloidal particles by composition and morphology as well as by size. The accuracy and precision of holographic characterization data are verified through validation measurements on particle-sizing standards with independently specified characteristics. Tracking the detection of individual particles in a known volume of flowing fluid yields measurements of the concentrations of each particle species in a sample. We demonstrate this capability with a model system composed of a mixture of latex microbeads, oil emulsion droplets and bacteria that is intended to resemble the effluent wastewater from petroleum refining. Holographic characterization successfully distinguishes the different types of colloidal particles in this heterogeneous dispersion and independently monitors their concentrations. These results illustrate the potential value holographic characterization for monitoring the quality of wastewater produced by a wide range of industrial and natural processes.

## Acknowledgements

This work was supported by the SBIR program of the National Science Foundation under grant number IIP-1519057 and the Higher Committee for Education Development (HCED) in Iraq.

## Appendix A. Supplementary data

Supplementary data related to this article can be found at http://dx.doi.org/10.1016/j.watres.2017.06.006.

## References

Adin, A., 1999. Particle characteristics: a key factor in effluent treatment and reuse. Water Sci. Technol. 40 (4–5), 67–74.
Aspnes, D.E., 1982. Local-field effects and effective-medium theory: a microscopic perspective. Am. J. Phys. 50, 704–709.
Berg, H.C., 2004. *E. coli* in Motion. Springer-Verlag, New York.
Bohren, C.F., Huffman, D.R., 1983. Absorption and Scattering of Light by Small Particles. Wiley Interscience, New York.
Bramucci, M., Nagarajan, V., 2006. Bacterial communities in industrial wastewater bioreactors. Curr. Opin. Microbiol. 9 (3), 275–278.
Cheong, F.C., Grier, D.G., 2010. Rotational and translational diffusion of copper oxide nanorods measured with holographic video microscopy. Opt. Express 18, 6555–6562.
Cheong, F.C., Sun, B., Dreyfus, R., Amato-Grill, J., Xiao, K., Dixon, L., Grier, D.G., 2009. Flow visualization and flow cytometry with holographic video microscopy. Opt. Express 17, 13071–13079.
Cheong, F.C., Xiao, K., Pine, D.J., Grier, D.G., 2011. Holographic characterization of individual colloidal spheres' porosities. Soft Matter 7, 6816–6819.
Crocker, J.C., Grier, D.G., 1996. Methods of digital video microscopy for colloidal studies. J. Colloid Interface Sci. 179, 298–310.
Dal Ferro, B., Smith, M., 2007. Global Onshore and Offshore Water Production. Oil and Gas Review, OTC edition.
Dixon, L., Cheong, F.C., Grier, D.G., 2011a. Holographic deconvolution microscopy for high-resolution particle tracking. Opt. Express 19, 16410–16417.
Dixon, L., Cheong, F.C., Grier, D.G., 2011b. Holographic particle-streak velocimetry.

Opt. Express 19, 4393–4398.
Goldburg, W., 1999. Dynamic light scattering. Am. J. Phys. 67 (12), 1152–1160.
Hannel, M., Middleton, C., Grier, D.G., 2015. Holographic characterization of imperfect colloidal spheres. Appl. Phys. Lett. 107, 141905.
Hawe, A., Schaubhut, F., Geidobler, R., Wiggenhorn, M., Friess, W., Rast, M., de Muynck, C., Winter, G., 2013. Pharmaceutical feasibility of sub-visible particle analysis in parenterals with reduced volume light obscuration methods. Eur. J. Pharm. Biopharm. 85 (3), 1084–1087.
Kasarova, S.N., Sultanova, N.G., Ivanov, D., Nikolov, I.D., 2007. Analysis of the dispersion of optical plastic materials. Opt. Mater. 29, 1481–1490.
Khelifa, A., Lee, K., Hill, P.S., 2004. Prediction of oil droplet size distribution in agitated aquatic environments. In: Artic and Marine Oilspill Program (AMOP) Technical Seminar, vol. 1. Environment Canada, p. 1046.
Kokal, S., et al., 2002. Crude oil emulsions: a state-of-the-art review. In: SPE Annual Technical Conference and Exhibition. Society of Petroleum Engineers, pp. 5–13.
Krishnatreya, B.J., Colen-Landy, A., Hasebe, P., Bell, B.A., Jones, J.R., Sunda-Meya, A., Grier, D.G., 2014. Measuring Boltzmann's constant through holographic video microscopy of a single sphere. Am. J. Phys. 82, 23–31.
Lee, S.-H., Grier, D.G., 2007. Holographic microscopy of holographically trapped three-dimensional structures. Opt. Express 15, 1505–1512.
Lee, S.-H., Roichman, Y., Yi, G.-R., Kim, S.-H., Yang, S.-M., van Blaaderen, A., van Oostrum, P., Grier, D.G., 2007. Characterizing and tracking single colloidal particles with video holographic microscopy. Opt. Express 15, 18275–18282.
Levine, A.D., Tchobanoglous, G., Asano, T., 1985. Characterization of the Size Distribution of Contaminants in Wastewater: Treatment and Reuse Implications. Water Pollution Control Federation, pp. 805–816.
Levine, A.D., Tchobanoglous, G., Asano, T., 1991. Size distributions of particulate contaminants in wastewater and their impact on treatability. Water Res. 25 (8), 911–922.
Liu, P.Y., Chin, L.K., Ser, W., Chen, H.F., Hsieh, C.-M., Lee, C.-H., Sung, K.-B., Ayi, T.C., Yap, P.H., Liedberg, B., Wang, K., Bourouina, T., Leprince-Wang, Y., 2016. Cell refractive index for cell biology and disease diagnosis: past, present and future. Lab a Chip 16, 634–644.
Liu, P.Y., Chin, L.K., Ser, W., Ayi, T.C., Yap, P.H., Bourouina, T., Leprince-Wang, Y., 2014. Real-time measurement of single bacterium's refractive index using optofluidic immersion refractometry. Procedia Eng. 87, 356–359.
Markwardt, C.B., 2009. Non-linear least squares fitting in IDL with MPFIT. In: Bohlender, D., Dowler, P., Durand, D. (Eds.), Astronomical Data Analysis Software and Systems XVIII. Astronomical Society of the Pacific, San Francisco, pp. 251–254.
Mishchenko, M.I., Travis, L.D., Lacis, A.A., 2001. Scattering, Absorption and Emission of Light by Small Particles. Cambridge University Press, Cambridge.
Murphy, F., Ewins, C., Carbonnier, F., Quinn, B., 2016. Wastewater treatment works (WwTW) as a source of microplastics in the aquatic environment. Environ. Sci. Technol. 50, 5800–5808.
Muttamara, S., 1996. Wastewater characteristics. Resour. Conserv. Recycl. 16 (1), 145–159.
Neves, A.A.R., Pisignano, D., 2012. Effect of finite terms on the truncation error of Mie series. Opt. Lett. 37, 2418–2420.
Office of Water (4303T), 2004. Effluent Guidelines Program Plan. Tech. Rep. EPA-821-R-04-014. U.S. Environmental Protection Agency.
Panchal, J., Kotarek, J., Marszal, E., Topp, E.M., 2014. Analyzing subvisible particles in protein drug products: a comparison of dynamic light scattering (DLS) and resonant mass measurement (RMM). AAPS J. 16 (3), 440–451.
Pena, O., Pal, U., 2009. Scattering of electromagnetic radiation by a layered sphere. Comput. Phys. Commun. 180, 2348–2354.
Rhyner, M.N., 2011. The coulter principle for analysis of subvisible particles in protein formulations. AAPS J. 13 (1), 54–58.
Sharma, D.K., King, D., Oma, P., Merchant, C., 2010. Micro-flow imaging: flow microscopy applied to sub-visible particulate analysis in protein formulations. AAPS J. 12 (3), 455–464.
Sheng, J., Malkiel, E., Katz, J., 2006. Digital holographic microscope for measuring three-dimensional particle distributions and motions. Appl. Opt. 45 (16), 3893–3901.
Shpaisman, H., Krishnatreya, B.J., Grier, D.G., 2012. Holographic microrefractometer. Appl. Phys. Lett. 101, 091102.
Tomaszewska, E., Soliwoda, K., Kadziola, K., Tkacz-Szczesna, B., Celichowski, G., Cichomski, M., Szmaja, W., Grobelny, J., 2013. Detection limits of DLS and UV-VIS spectroscopy in characterization of polydisperse nanoparticles colloids. J. Nanomater. 2013, 60.
Wang, C., Cheong, F.C., Ruffner, D.B., Zhong, X., Ward, M.D., Grier, D.G., 2016a. Holographic characterization of colloidal fractal aggregates. Soft Matter 12, 8774–8780.
Wang, C., Zhong, X., Ruffner, D.B., Stutt, A., Philips, L.A., Ward, M.D., Grier, D.G., 2016b. Holographic characterization of protein aggregates. J. Pharm. Sci. 105, 1074–1085.
Weinbuch, D., Jiskoot, W., Hawe, A., 2014. Light obscuration measurements of highly viscous solutions: sample pressurization overcomes underestimation of subvisible particle counts. AAPS J. 16 (5), 1128–1131.
Wiscombe, W.J., 1980. Improved Mie scattering algorithms. Appl. Opt. 19, 1505–1509.
Xu, R., 2001. Particle Characterization: Light Scattering Methods. Particle Technology Series. Kluwer Academic Publishers, Dordrecht.
Xu, R., 2015. Light scattering: a review of particle characterization applications. Particuology 18, 11–21.
Yang, W., 2003. Improved recursive algorithm for light scattering by a multilayered sphere. Appl. Opt. 42, 1710–1720.
Yevick, A., Hannel, M., Grier, D.G., 2014. Machine-learning approach to holographic particle characterization. Opt. Express 22, 26884–26890.
Yu, L., Han, M., He, F., 2013. A review of treating oily wastewater. Arab. J. Chem. http://dx.doi.org/10.1016/j.arabjc.2013.07.020.